Available online at www.sciencedirect.com

ScienceDirect

journal homepage: www.elsevier.com/locate/he

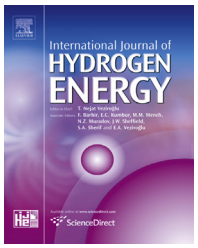

Real-time monitoring of a micro reformer integrated with a microchannel heat exchanger by infrared thermography and high-speed flow images

Ben-Ran Fu [a], *Yu-Chia Ting* [b], *Cheng-Fong Lee* [b], *Yuh-Jeen Huang* [c], *Yu-Chuan Su* [b], *Fan-Gang Tseng* [b], *Chin Pan* [b,d,e,*]

[a] *Department of Mechanical Engineering, Ming Chi University of Technology, New Taipei City, Taiwan*
[b] *Department of Engineering and System Science, National Tsing Hua University, Hsinchu, Taiwan*
[c] *Department of Biomedical Engineering and Environmental Sciences, National Tsing Hua University, Hsinchu, Taiwan*
[d] *Institute of Nuclear Engineering and Science, National Tsing Hua University, Hsinchu, Taiwan*
[e] *Low Carbon Energy Research Center, National Tsing Hua University, Hsinchu, Taiwan*

ARTICLE INFO

Article history:
Received 23 December 2015
Received in revised form
5 August 2016
Accepted 6 August 2016
Available online 29 August 2016

Keywords:
Thermal image
Two-phase flow evolution
POM reaction
Hydrogen generation

ABSTRACT

This study develops a silicon-based microfluidic device incorporating a micro reformer that employs the partial oxidation of methanol (POM) reaction and a microchannel heat exchanger (MCHE) for potential reforming methanol fuel cell application. Two-dimensional temperature distribution of the reformer and two-phase flow evolution in the MCHE are acquired by infrared (IR) thermography and high-speed digital camera images, respectively. The composition of gas products is further analyzed by gas chromatography. The maximal hydrogen production rate of 2.97×10^{-5} mol/s and selectivity of 77.3% are obtained in the present study. Thermal images of the reformer indicate that the POM reaction is more intense near the outlet, and the high-temperature region expands from the outlet to inlet regions with time until the steady state is reached. The present study reveals that IR thermography with proper calibration facilitates real-time temperature monitoring, which enables understanding the distribution of the reforming reaction and its evolution through the reformer until the steady state is reached. The shortest time for approaching the steady state is only 8 s for the present system under certain conditions. The data obtained may provide a basis for theoretical and numerical analyses on the progress of temperature and reforming reaction. In addition, the present results demonstrate that the micro evaporator may effectively use the heat produced from the exothermic POM reaction and provide low-temperature hydrogen for possible application in fuel cells.

* *Corresponding author*. Department of Engineering and System Science, National Tsing Hua University, Hsinchu, Taiwan. Fax: +886 3 572 0724.
E-mail addresses: brfu@mx.nthu.edu.tw (B.-R. Fu), cpan@ess.nthu.edu.tw (C. Pan).
http://dx.doi.org/10.1016/j.ijhydene.2016.08.023
0360-3199/

Introduction

Fuel cells, which generate electricity and heat through electrochemical reactions, are basically open thermodynamic systems [1]. Based on the type of reactant and electrolyte [2], fuel cells can be classified into the following six categories: alkaline fuel cell, phosphoric acid fuel cell, solid oxide fuel cell, molten carbonate fuel cell, proton exchange membrane fuel cell (PEMFC), and direct methanol fuel cell (DMFC). Portable applications of fuel cells mainly include portable power generators for outdoor uses and power supply for consumer electronic devices [3]. PEMFC and DMFC are appropriate candidates for portable applications because of their silent operation, high power and energy density, and low relative weight. Reforming methanol fuel cells (RMFCs) are also attractive candidates for portable applications and have been extensively studied in the literature recently [4–7]. Avgouropoulos et al. [4] stated that RMFCs have several merits: simplification of the fuel processor–fuel cell unit; cost effective and safe operation; and higher energy densities due to methanol as a primary hydrogen carrier. In RMFCs, methanol is reformed to hydrogen, which is then fed into the fuel cell (such as PEMFC). Huang et al. [8] and Wang et al. [6] examined the partial oxidation of methanol (POM) reaction, which is a typical chemical reaction employed in the RMFC and can be generalized as follows: $CH_3OH + 0.5O_2 \rightarrow 2H_2 + CO_2$. The POM reaction is an exothermic process in which the temperature of the gas products is generally around 200 °C.

The temperature distribution in the fuel cell might be non-uniform, and the thermal management of the fuel cell system is a critical issue. Numerous studies have numerically investigated the temperature distribution of the fuel cell system [9–11]. However, a few studies have experimentally examined the temperature distribution in the reformer. For example, using embedded micro temperature sensors, Lee et al. [12] experimentally measured the local temperature distribution in a micro reformer that employed the steam reforming of methanol (SRM) reaction. Unlike the POM reaction, the SRM reaction, i.e., $CH_3OH + H_2O \rightarrow 3H_2 + CO_2$, is endothermic. Therefore, RMFC systems employing the SRM reaction are generally accompanied by an external heater to meet the heat requirement. The operation temperature of the reformer of the RMFC system in Lee et al. [12] was 240–300 °C. Their experimental results demonstrated that the temperature upstream of the reformer declined more rapidly than that midstream and downstream. This is because the endothermic reaction upstream of the reformer is much more intense than that in other regions.

In recent years, many studies have used infrared (IR) thermography for fuel cell systems to serve different purposes, such as measuring the thermal field or temperature distribution [13–16], detecting the failure point [17,18], or monitoring system leakage [19]. In general, IR thermography has the following merits [20]: non-contact and non-invasive technology; two-dimensional thermal images; real-time measurement; and no harmful radiation effects of other technologies (such as X-ray imaging). Usamentiaga et al. [21] conducted a detailed review on the principles of IR thermography and its applications in temperature measurement and non-destructive testing.

The present study develops a silicon-based microfluidic device including a micro reformer and microchannel heat exchanger (MCHE) for potential RMFC application. The POM reaction is employed in the reformer coated with Cu-Mn-Zn as the catalyst. The real-time temperature distribution of the reformer was monitored by IR thermography, and the two-phase flow evolution of methanol in the MCHE was captured with a high-speed digital camera. In addition, the composition of gas products was further analyzed by gas chromatography, which enables evaluating production rate and selectivity. The effects of methanol flow rate, oxygen flow rate, and heating power on the characteristics of the reformer, especially the dynamic temperature distribution, were investigated.

Experimental details

Experimental setup

Fig. 1 illustrates the experimental setup of the present study, including a test section, a syringe pump (KD SCIENTIFIC, model: 200), a gas tank with a mass flow controller (TOKYO KEISO, model: NM2100DC), a power supply, an IR thermography (FLIR, model: SC655), a high-speed digital camera (IDT, model: MotionPro X4) mounted with a microlens (OPTEM, model: Zoom 125C) and a metal halide light source (HAYASHI, model: LA-60Me-R), a gas chromatography (CHINA CHROMATOGRAPHY, model: GC2000), a data acquisition system (YOKOGAWA, model: MX100), and computers. The data acquisition system, connected to the computer, recorded the signals from T-type thermocouples with ±0.2 °C uncertainty.

The test section, as shown in Fig. 2, was assembled with a micro reformer and an MCHE (serving as an evaporator) with an external heater connected to the power supply. Fig. 3 further displays a schematic of the micro reformer integrated with the MCHE and detailed flow paths of the reactants and products therein. The reformer of dimensions 20 × 20 mm^2, in which the active area is 16 × 15 mm^2, comprises five microchannels with a finger-shaped microstructure design. The channel depth of the reformer is 350 μm, and the channel wall is coated with Cu-Mn-Zn as the catalyst for the POM reaction. The detailed methods for catalyst preparation and its coating procedure in the reformer have been described in Lee et al. [22] and Wang et al. [6], respectively. The finger-shaped design of the reformer could increase the reaction area and the resident time of the reactant and eventually the conversion rate of methanol, as demonstrated by Wang et al. [6]. In the present study, the reforming reaction occurs at 150–250 °C and the reformer is heated from the bottom, especially during the startup period, by the external heater.

The MCHE utilizes the residual heat of the gas products from the reformer as well as the heat from the heater below the reformer to vaporize the methanol in the mixture of liquid methanol and oxygen gas. Consequently, the residual heat can be recovered and the temperature of the gas products from the reformer can be lowered to the appropriate temperature for use in the fuel cell. A fuel cell was not integrated in the present study. The MCHE is fabricated on a silicon wafer. The hot side of the MCHE, which has 18 uniform cross-section microchannels, is used for the flow of gas products.

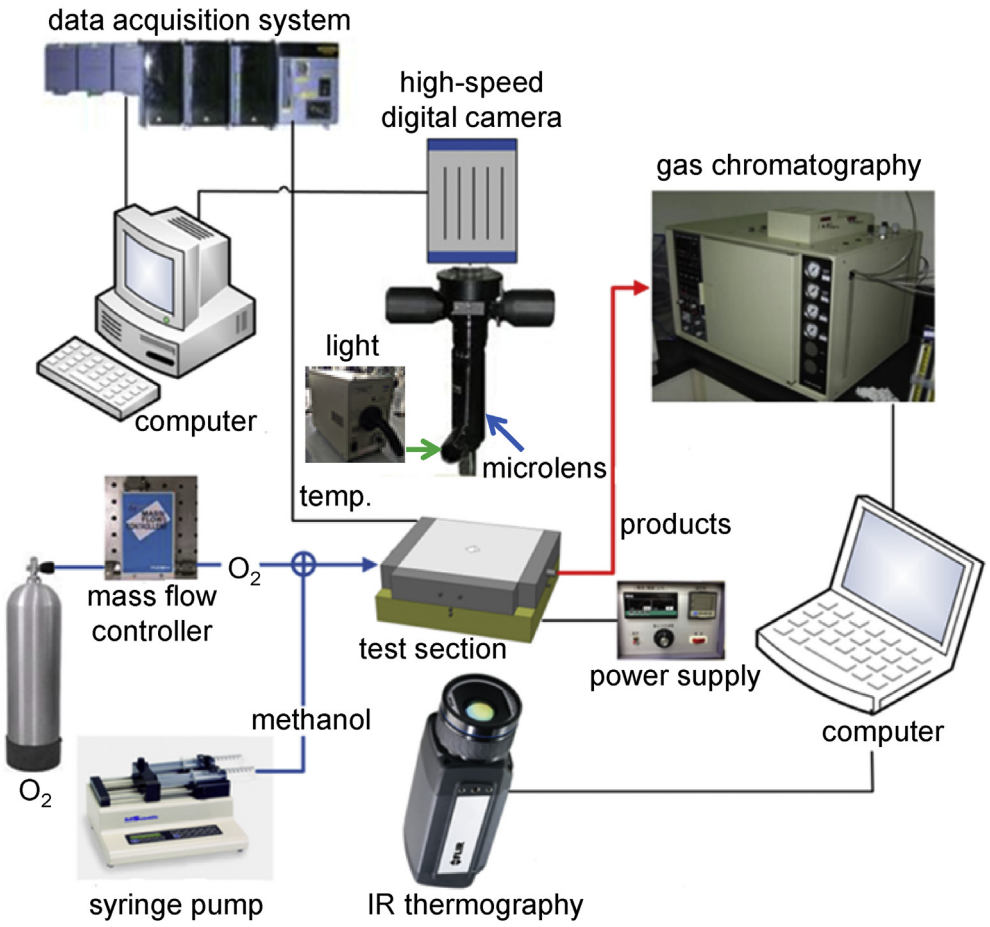

Fig. 1 – Test rig of the experiments.

The channel width, depth, and length are 300 μm, 200 μm, and 10.5 mm, respectively. On the other hand, the cold side for the vaporization of methanol employs a diverging cross-section design with a channel width of 250 μm at the inlet and 350 μm at the exit. The depth of all 18 parallel channels is 200 μm. The channel length on the cold side is also 10.5 mm. Such a diverging microchannel design could stabilize the boiling two-phase flow and enhance the boiling heat transfer [23,24].

The liquid methanol is driven by the syringe pump at a given flow rate into the test section with oxygen gas (99.999% purity) from the high-pressure tank through the mass flow controller. The methanol in the mixture is then vaporized in the MCHE using the high-temperature gas products, mainly hydrogen, from the reformer. The mixture of methanol vapor and oxygen gas subsequently flow into the micro reformer to partially oxidize methanol with the catalyst coated on the channel wall of the reformer.

The two-phase flow pattern during the boiling of the methanol and oxygen mixture in the MCHE is visualized using the high-speed digital camera. A window of dimensions 10×10 mm^2 is designed for two-phase flow visualization, as shown in Fig. 2. In addition, the camera is mounted on an x–y–z mechanism to hold the lens and provide accurate positioning and focusing. The high-speed digital camera captured images at a typical frame rate of 1000 frame/s. In addition, the reformer temperature during the reaction is monitored by the IR thermography from the back side, which is coated with a graphite tape. A through hole of diameter 10 mm at the center of the heater, as shown in Fig. 2, is designed as the window for IR thermography. The IR thermography used in the present study is suitable for temperature measurement in the range 100–650 °C with ±2% uncertainty and a resolution of 640 × 480 pixels. The typically used frame rate of the IR thermography is 25 frame/s during the experiment.

Fabrication of the reformer and MCHE

Microelectromechanical systems (MEMS) technology was employed to fabricate the micro reformer and MCHE because of its compatibility with silicon-based RMFC systems, which will be developed in the future. MEMS technology has been widely used to fabricate micro fuel cell systems [25–31], which might include a micro combustor, micro reformer, micro heat exchanger, micro sensor, and fuel/oxidant cartridge. In the present study, the micro reformer and MCHE were separately fabricated on a p-type <100> silicon wafer of thickness 0.5 mm. The fabrication process of the MCHE includes the following main steps: (1) cleaning the wafer and spin coating a positive photoresist onto the wafer; (2) using photolithography and silicon dry etching to fabricate the patterns on the wafer; (3) stripping the photoresist from the wafer and repeating steps (1) and (3) to develop the patterns on the other

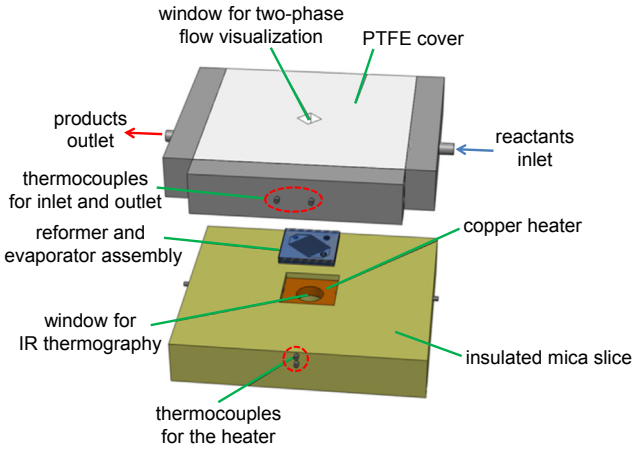

(a) Exploded drawing

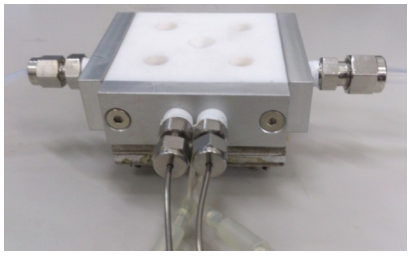

(b) Appearance of the test section

Fig. 2 – Test section assembly.

side; (4) applying anodic bonding to cover a 0.6-mm-thick Pyrex 7740 glass on the wafer for flow visualization; and finally, (5) cutting the wafer to form a chip of the device. In addition, the inlets, outlets, and through holes of the device were drilled into the Pyrex 7740 glass and wafer by laser micromachining prior to anodic bonding. The fabrication process of the micro reformer is the same as that of the MCHE, except that it does not fabricate the backside structure (i.e., excluding step (3)). Fig. 3(b) shows the final appearances of the MCHE (combining layers 1 and 2 in Fig. 3(a)) and micro reformer (combining layers 3 and 4 in Fig. 3(a)). After embedding the catalyst in the reformer, the MCHE and reformer were further combined by anodic bonding, resulting in a microfluidic device comprising four stacked layers of dimensions 20 mm (width) × 20 mm (length) × 2.2 mm (thickness), as shown in Fig. 3(a) (i.e., Pyrex 7740, MCHE, Pyrex 7740, and micro reformer).

Calibration of IR measurements

The temperature measurement from the IR thermography is calibrated using a silicon wafer sample and a thermocouple as follows. The polished side of the silicon wafer sample of dimensions 20 × 20 mm^2 is attached with a T-type thermocouple using graphite colloidal, while the back side of the sample is coated with a graphite tape to maximize its emissivity. As the silicon wafer is very thin, it may be considered a lumped object and the temperature on both sides would be approximately the same. This silicon wafer sample is heated by the heating module, and then, the temperature measured by the IR thermography can be compared with that by the attached thermocouple. Fig. 4 illustrates the calibration curve, which can be fitted very well by the following linear equation:

$$T = 0.976T_R + 4.82\ (^{\circ}C) \quad (1)$$

where T_R is the temperature obtained from the IR thermography and T is the temperature measured by the thermocouple. Based on this calibration equation, the uncertainty of the temperature measured by the IR thermography ranges from −2.42% to +1.65%, which is very close to the original manufacturer specifications (i.e., ±2%) for the target temperature range 100–650 °C. This result further indicates that the present calibration method for IR measurement is appropriate.

Experimental procedure

With the methanol flow rate (Q_{MeOH}) fixed at 0.25 ml/min and heating power (q_H) fixed at 21.25 W, the oxygen flow rate (Q_{Oxy}) is varied as 4, 6, 8, and 10 sccm to find Q_{Oxy} with the highest hydrogen production rate and hydrogen selectivity. Subsequently, at this Q_{Oxy} and Q_{MeOH} of 0.04 ml/min, the effects of q_H on the temperature distribution and hydrogen production rate are further investigated. For each set of Q_{MeOH}, Q_{Oxy}, and q_H, various data are recorded after the initial transient of about 1 h. The data acquisition system records the fluid temperature at the inlet and outlet and the heater temperature, as indicated in Fig. 2(a). The two-phase flow pattern in the evaporator is captured using the high-speed digital camera. In addition, the temperature of the micro reformer is recorded using the IR thermography. After the initial transient, the gas products are collected using a gas sampling bag for about 1 h. The gas sampling bag is weighed using an electronic balance to facilitate its analyses later. Subsequently, it is heated using a heating plate to 120 °C for about 30 min to ensure that the liquid methanol and water possibly condensed in the bag are fully vaporized. It is then sampled for 100 μl using a leak-proof syringe needle for a detailed composition analysis using the gas chromatography.

Results and discussion

Composition analysis of products

In general, the performance of the reformer employed as a hydrogen supplier can be evaluated by the production rate and hydrogen and carbon monoxide selectivities:

$$H_2\ \text{selectivity}\ (\%) = m_{H_2}/(m_{H_2} + m_{H_2O}) \times 100 \quad (2)$$

$$CO\ \text{selectivity}\ (\%) = m_{CO}/(m_{CO} + m_{CO_2}) \times 100 \quad (3)$$

where m is the mole of the component in the sample. For a desirable methanol reformer, the hydrogen production rate and selectivity should be high. In contrast, these parameters should be as low as possible for carbon monoxide. In addition, the existence of carbon monoxide may poison the catalyst of the fuel cell system, especially the platinum in PEMFC and DMFC.

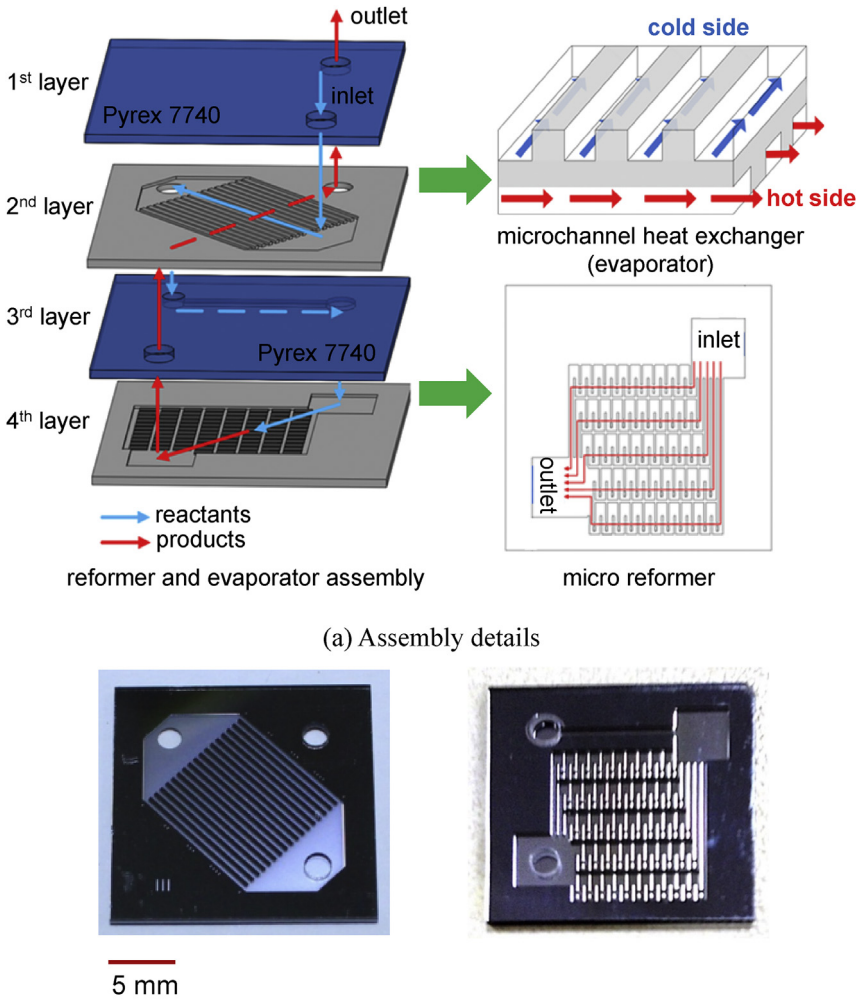

Fig. 3 – Micro reformer integrated with a MCHE and detailed flow paths of reactants and products therein.

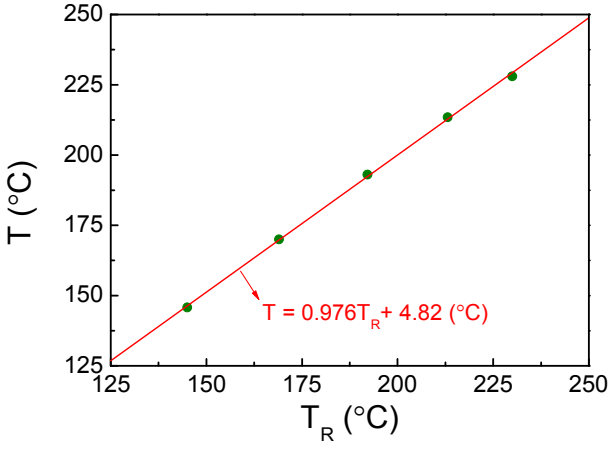

Fig. 4 – Calibration curve for the temperature measurement.

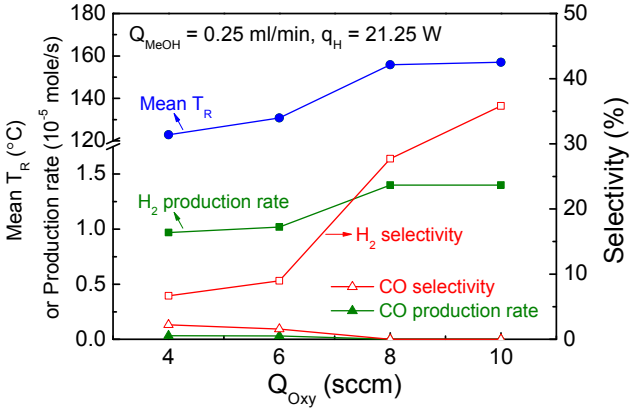

Fig. 5 – Effect of oxygen flow rate on production rate, selectivity, and corresponding mean temperature at Q_{MeOH} = 0.25 ml/min and q_H = 21.25 W.

Fig. 5 presents the results for the production rate, selectivity, and corresponding mean temperature at Q_{MeOH} = 0.25 ml/min, which is much higher than the one corresponding to the stoichiometry ratio of the POM reaction at Q_{Oxy} = 10 sccm and q_H = 21.25 W. Here, the mean temperature is based on the average inlet-to-outlet line temperature of the reformer. This figure shows that the mean temperature of the reformer increases as Q_{Oxy} increases, which presents a similar trend to the

report of Chen and Shen [32], who studied the POM reaction with a different catalyst (i.e., Pt/Al_2O_3) at a high reaction temperature (up to 692 °C). The results further reveals that the hydrogen production rate increases slightly from 0.97×10^{-5} to 1.02×10^{-5} mol/s as Q_{Oxy} increases from 4 to 6 sccm, but it increases rapidly from 1.02×10^{-5} to 1.40×10^{-5} mol/s as Q_{Oxy} increases from 6 to 8 sccm. In addition, no significant difference in the hydrogen production rate is presented at Q_{Oxy} of 8–10 sccm. This figure also shows a highly positive relationship between the mean temperature of the reformer and the hydrogen production rate as Q_{Oxy} changes. In contrast, the production rate of carbon monoxide decreases monotonically with increasing Q_{Oxy}. In particular, at $Q_{Oxy} = 8$ and 10 sccm, the carbon monoxide yield is less than the detected limitation of the present gas chromatography, resulting in no analytical data for these two cases. Fig. 5 further demonstrates that for increasing hydrogen selectivity at given Q_{MeOH} and q_H, increasing Q_{Oxy} is considerably efficient. However, the maximal hydrogen selectivity is only 35.8%, much lower than that (i.e., >70%) in Wang et al. [6]. This is due to both the lower temperature of the reformer (≤157 °C) and the higher flow rate of reactants (i.e., shorter resident time) than those reported in Wang et al. [6], where the reformer temperature was 180–250 °C at $Q_{MeOH} = 0.02$ ml/min and $Q_{Oxy} = 6.1$ sccm.

The above results indicate that $Q_{Oxy} = 10$ sccm results in the highest hydrogen production rate as well as selectivity. At this oxygen flow rate and its corresponding stoichiometry ratio of Q_{MeOH} for the POM reaction, the effect of heating power, q_H, is further investigated. Fig. 6 shows the effect of q_H on the production rate, selectivity, and corresponding mean temperature at $Q_{Oxy} = 10$ sccm and $Q_{MeOH} = 0.04$ ml/min, which is the corresponding ratio of the POM reaction. This figure demonstrates that the hydrogen production rate increases from 0.53×10^{-5} to 0.83×10^{-5} mol/s as q_H increases from 22.5 to 23.75 W, and then, it decreases slightly from 0.83×10^{-5} to 0.75×10^{-5} mol/s as q_H increases from 22.5 to 23.75 W. The mean temperature of the reformer ranges from 215 °C to 235 °C, much higher than that at $Q_{MeOH} = 0.25$ ml/min. In addition, carbon monoxide could not be quantitatively measured in the gas chromatography, resulting in no production rate and selectivity for carbon monoxide under this operation condition. Fig. 6 also shows that the hydrogen selectivity decreases slightly from 77.3% to 73.5% as q_H increases from 22.5 to 23.75 W, and it drops dramatically from 73.5% to 26.2% as q_H increases from 23.75 to 25 W. This result indicates that the increase in q_H significantly decreases the hydrogen selectivity at a given flow rate of reactants while the reformer temperature is sufficiently high. Moreover, in the present study, the maximal hydrogen selectivity at $Q_{MeOH} = 0.04$ ml/min is much higher than that at $Q_{MeOH} = 0.25$ ml/min, which results from the differences in the resident time of methanol and reformer temperature. In general, a longer resident time of methanol and higher reformer temperature result in higher conversion of methanol and hydrogen selectivity.

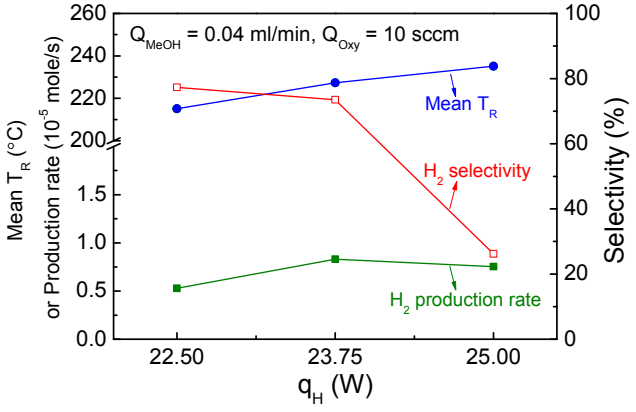

Fig. 6 – Effect of heating power on production rate, selectivity, and corresponding mean temperature at $Q_{MeOH} = 0.04$ ml/min and $Q_{Oxy} = 10$ sccm.

Based on the above findings, we conducted another experiment to obtain a larger yield of hydrogen at $Q_{MeOH} = 0.25$ ml/min, $Q_{Oxy} = 10$ sccm, and $q_H = 22.5$ W. In this case, the hydrogen production rate reaches 2.97×10^{-5} mol/s, which is about 212% of that at the same given flow rate of reactants but with $q_H = 21.25$ W. In addition, the hydrogen selectivity increases from 35.8% to 47.2% as q_H increases slightly from 21.25 to 22.5 W. Table 1 summarizes the detailed operation conditions and results for the highest hydrogen production rate and selectivity in the present study. The outlet temperatures of fluid (products and others) at the outlet of the methanol evaporator are 117.8 °C and 126.6 °C, respectively, in these two cases. Although the reformer temperature is greater than 200 °C, the outlet temperature successfully drops to an acceptable level for potential application in PEMFC or DMFC, which indicates the practicability of the design of the present microfluidic device.

High-speed flow images in the MCHE

Fig. 7 presents the three typical two-phase flow patterns, namely (a) bubbly slug flow, (b) annular flow, and (c) liquid film breakup with dryout occurrence, captured by the high-speed digital camera in the MCHE. These flow patterns are observed at $Q_{MeOH} = 0.25$ ml/min and $q_H = 21.25$ W. In general, the bubbly slug flow is presented in the region near the entrance of the MCHE, followed by the coalescence of bubbles

Table 1 – Operation conditions and results for the highest hydrogen production rate (Case A) and selectivity (Case B).

Parameters	Case A	Case B
Methanol flow rate, Q_{MeOH} (ml/min)	0.25	0.04
Oxygen flow rate, Q_{Oxy} (sccm)	10	10
Heating power, q_H (W)	22.5	22.5
Mean temperature in the reformer, T_R (°C)	168.6	215.1
Uniformity of reformer temperature	Low	High
Evaporator inlet temperature of fluid (°C)	95	102.2
Evaporator outlet temperature of fluid (°C)	117.8	126.6
Location of dryout occurrence	Inside MCHE	Inlet of MCHE
H_2 production rate (10^{-5} mol/s)	2.97	0.529
H_2 selectivity (%)	47.2	77.3

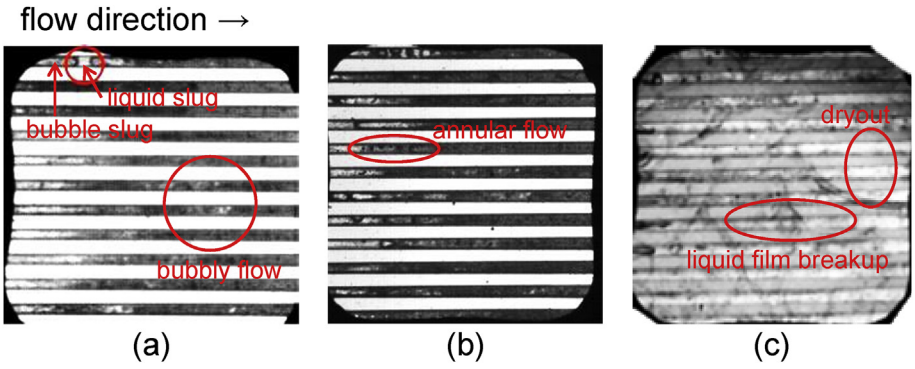

Fig. 7 – Typical two-phase flow patterns in the MCHE at Q_{MeOH} = 0.25 ml/min and q_H = 21.25 W: (a) bubbly-slug flow, (b) annular flow, and (c) liquid film breakup with dryout occurrence.

forming an annular flow, and finally, the liquid film breakup accompanied with dryout near the exit of the MCHE. Fig. 7 also shows that an entrainment of liquid droplets is frequently observed in the annular flow owing to additional shear force caused by oxygen flowing through the MCHE, which is much different from the annular flow observed in the microchannel during the boiling process of methanol without oxygen, as reported by Fu et al. [33]. In addition, the visualization results show that the dominant flow pattern in the MCHE is the bubbly slug flow at $Q_{Oxy} \leq 6$ sccm and the annular flow at $Q_{Oxy} \geq 8$ sccm. In contrast, the above-mentioned flow patterns are not observed at Q_{MeOH} = 0.04 ml/min because dryout always occurs in the inlet of the MCHE. The two-phase flow characteristics of the present microchannel is strongly linked with the thermal field of the micro reformer, as the later provides the reaction heat, together with the heat from the heater, for the evaporation of methanol. The low heat dissipation and the poor heat transfer after dryout lead to the high overall temperature of the reformer at this low methanol flow rate, which can be observed in the thermal images of the reformer in the following section. The detailed heat transfer characteristics and two-phase flow evolutions during the phase change of the methanol in the MCHE with co- and counter-current flow arrangements by high-temperature gas heating have been explored in our previous studies [34,35]. The present MCHE was designed with the same geometries but a different flow arrangement (i.e., cross flow) to match the system layout with the designed reformer.

Thermal image of the reformer

Fig. 8 shows the evolution of the thermal images, captured by the IR thermography, of the reformer for different oxygen flow rates (i.e., Q_{Oxy} = 4–10 sccm) at Q_{MeOH} = 0.25 ml/min and q_H = 21.25 W. The monitoring region, at the reformer's backside, is the circular area between the inlet and outlet, as indicated in the first drawing under Fig. 8(a). From the beginning to the steady state, the temperature ranges of the monitoring region in the cases with Q_{Oxy} of 4, 6, 8, and 10 sccm are 114.0–127.1 °C, 117.4–137.0 °C, 150.0–159.3 °C, and 150.6–159.4 °C, respectively, with low temperature near the inlet and high temperature near the outlet. The thermal images indicate that the reforming reaction is more intense near the outlet and the high-temperature region there expands from the outlet to the inlet region with time. As the POM method adopted in this study is exothermic, the reaction heat produced in the upstream region as well as the heat from the external heater will be carried to the downstream region with the flow and make the reaction there more intensive, and consequently, produce more heat. This elevates the temperature near the outlet and creates a temperature field for thermal conduction to the region nearby. This then increases the reaction and temperature nearby. This process goes on until the steady state is reached. The more intense exothermic POM reaction in the downstream region in this study contradicts that reported by Lee et al. [12], who employed the endothermic SRM reaction and found that the reaction is more intense in the upstream region.

Fig. 8 also indicates that the time required to reach the steady reformer temperature is less than 24 s for this high flow rate of methanol; in particular, it is only 8 s at Q_{Oxy} = 10 sccm. This figure demonstrates that at a given Q_{MeOH} and q_H, the mean temperature of the reformer increases with increasing Q_{Oxy} as well as time. In addition, the increase in the reformer temperature is most significant as Q_{Oxy} increases from 6 to 8 sccm. At Q_{Oxy} = 10 sccm, as shown in Fig. 8(d). The temperature distribution develops quite uniformly in only 8 s, which indicates that a higher Q_{Oxy} yields better temperature uniformity in the reformer at given Q_{MeOH} and q_H. This might also be beneficial to the heat transfer process in the MCHE of the microfluidic device.

Fig. 9 further presents the detailed evolution of temperature distribution along the diagonal line from the reformer inlet to the outlet, as illustrated in the drawing under Fig. 8(a), for different oxygen flow rates (Q_{Oxy} = 6 and 10 sccm) at Q_{MeOH} = 0.25 ml/min and q_H = 21.25 W. This figure shows that at t = 20 and 24 s, the temperature distributions at Q_{Oxy} = 6 sccm are very close to each other, indicating that the system has approached the steady state at t = 24 s, while the steady state is reached much sooner at t = 8 s and Q_{Oxy} = 10 sccm. Moreover, this figure clearly shows that the temperature in the reformer at Q_{Oxy} = 10 sccm is much more uniform than that at Q_{Oxy} = 6 sccm. The mean temperature of this line at Q_{Oxy} = 6 sccm and t = 24 s is 130.8 ± 6.1 °C while it is 157.0 ± 3.4 °C at Q_{Oxy} = 10 sccm and t = 8 s. In addition, the mean temperature increases with time and the increases in the mean temperature are 7.3 °C and 2.2 °C at Q_{Oxy} = 6 and 10 sccm, respectively, as the steady state is reached.

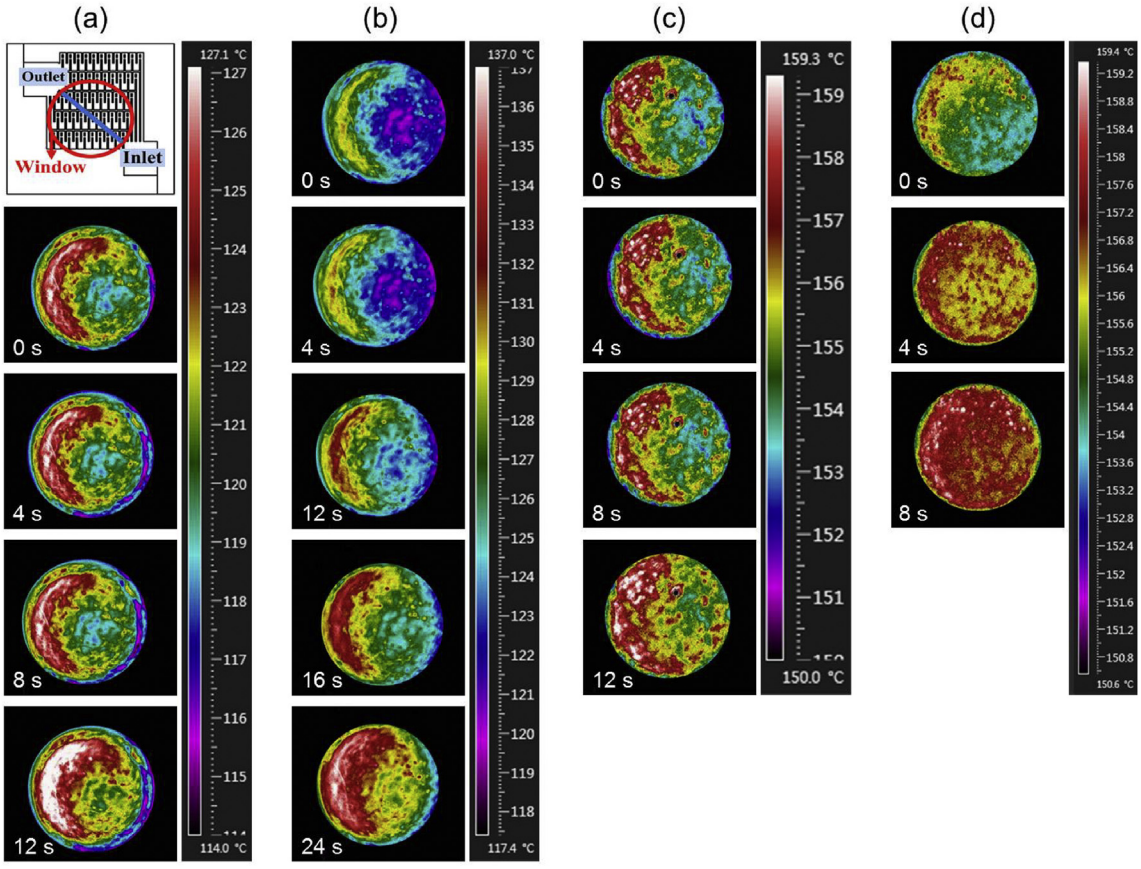

Fig. 8 – Evolution of thermal images of the reformer for different oxygen flow rates: (a) 4 sccm, (b) 6 sccm, (c) 8 sccm, and (d) 10 sccm, at Q_{MeOH} = 0.25 ml/min and q_H = 21.25 W.

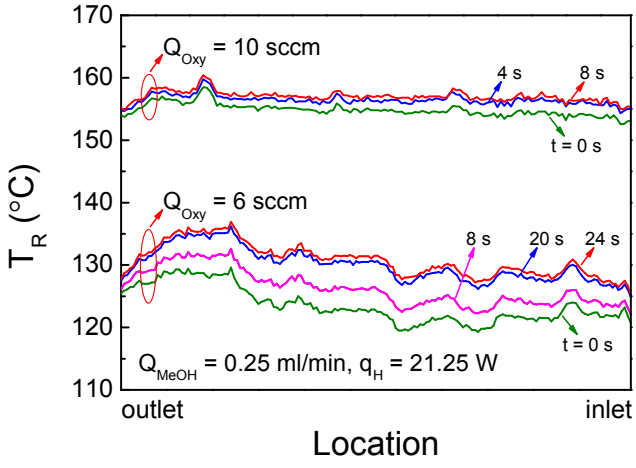

Fig. 9 – Evolution of temperature distribution along the inlet-to-outlet line of the reformer for the different oxygen flow rates (Q_{Oxy} = 6 and 10 sccm) at Q_{MeOH} = 0.25 ml/min and q_H = 21.25 W.

To further study the effect of q_H on the evolution of temperature distribution in the reformer, the experiments were also conducted at Q_{Oxy} = 10 sccm and Q_{MeOH} = 0.04 ml/min, which is much lower than that in the previous case (i.e., 0.25 ml/min). Fig. 10 shows the evolution of the thermal images of the reformer for different heating powers (i.e., q_H = 22.5–25 W). The temperature ranges of the monitoring region in the cases with q_H of 22.5, 23.75, and 25 W are 210.0–220.3 °C, 219.1–229.1 °C, and 221.0–239.9 °C, respectively. The thermal images demonstrate that the required time to reach the steady condition of the reformer temperature decreases rapidly from 283 to 100 s as q_H increases from 22.5 to 25 W. Moreover, the time needed for these three cases with Q_{MeOH} = 0.04 ml/min is much longer than that with Q_{MeOH} = 0.25 ml/min (i.e., only about 24 s, as shown in Fig. 8). This is because for the present micro evaporator, such a small methanol flow rate of 0.04 ml/min results in large amplitude, low-frequency thermal and flow oscillations, as demonstrated by the temperature oscillation at the evaporator inlet in Fig. 11. The mean temperatures of the reformer in these three cases with Q_{MeOH} = 0.04 ml/min are also considerably higher than that with Q_{MeOH} = 0.25 ml/min. This is because of the low heat transfer to the methanol evaporator as the heat dissipation for the phase change of methanol is much lower at this methanol flow rate and the earlier occurrence of dryout at or near the inlet, as demonstrated by the boiling visualization, resulting in poor heat transfer to the vapor flow.

Summary and conclusions

For potential reforming methanol fuel cell application, this study developed a microfluidic device incorporating a micro

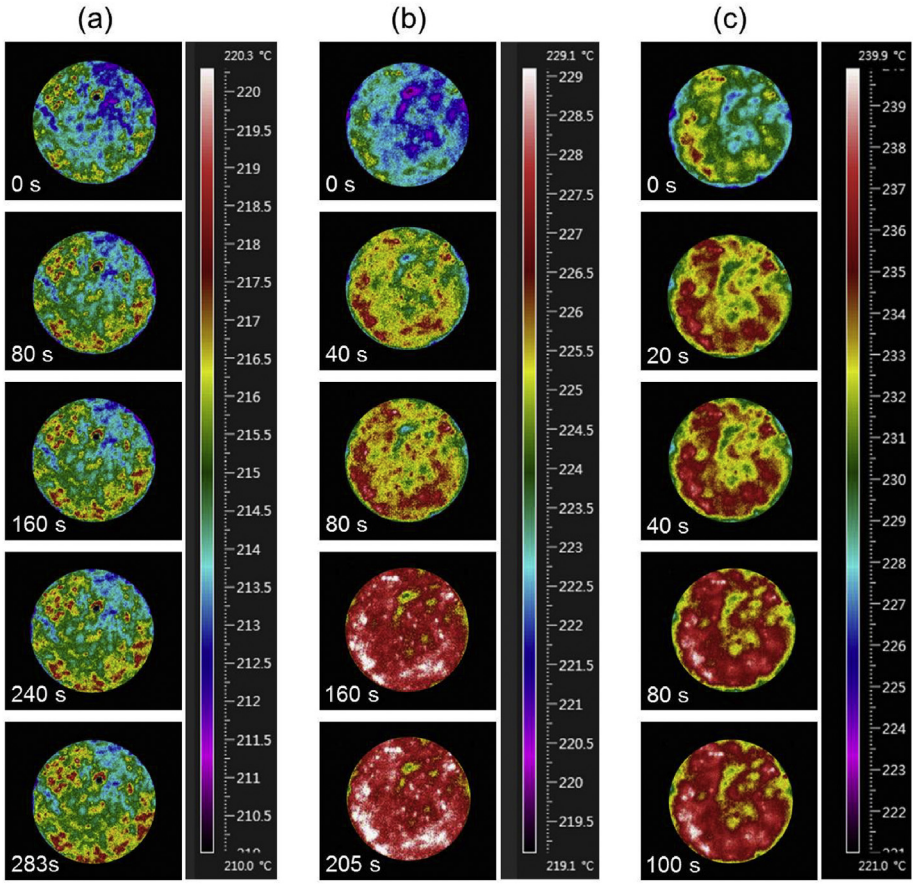

Fig. 10 – Evolution of thermal images of the reformer for different heating powers: (a) 22.5 W, (b) 23.75 W, and (c) 25 W, at Q_{MeOH} = 0.04 ml/min and Q_{Oxy} = 10 sccm.

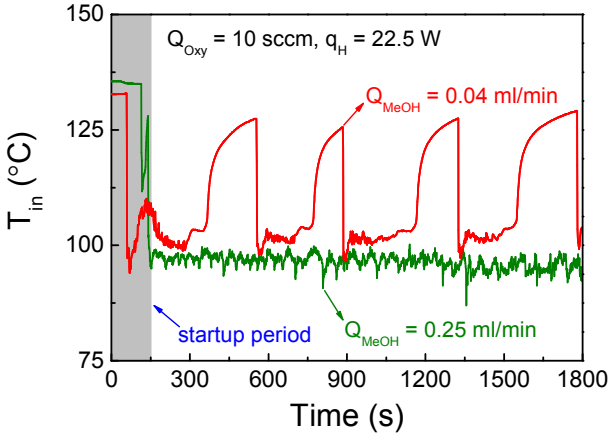

Fig. 11 – Characteristic of temperature oscillation at the evaporator inlet for different methanol flow rates.

reformer that employs the POM reaction and an MCHE. Two-dimensional temperature distribution of the reformer and two-phase flow evolution in the MCHE are acquired by IR thermography and high-speed digital camera images, respectively. The composition of gas products is further analyzed by gas chromatography. The primary findings of the present study are summarized as follows:

(1) The maximal hydrogen production rate of 2.97×10^{-5} mol/s and selectivity of 77.3% are obtained for the case with Q_{MeOH} = 0.25 and 0.04 ml/min, respectively, at Q_{Oxy} = 10 sccm and q_H = 22.5 W. At given Q_{MeOH} and q_H, the hydrogen production rate increases slightly as Q_{Oxy} increases from 4 to 6 sccm, but it increases rapidly as Q_{Oxy} increases from 6 to 8 sccm; in addition, no obvious difference in the hydrogen production rate is presented between Q_{Oxy} = 8 and 10 sccm. The shortest time for approaching the steady state is only 8 s corresponding to the condition of Q_{Oxy} = 10 sccm. At given flow rates of reactants, the hydrogen selectivity decreases slightly from 77.3% to 73.5% as q_H increases from 22.5 to 23.75 W, and it drops dramatically from 73.5% to 26.2% as q_H further increases from 23.75 to 25 W.

(2) In general, the bubbly slug flow is presented in the region near the entrance of the MCHE, followed by the coalescence of bubbles forming annular flow, and finally, the liquid film breakup accompanied with dry-out near the exit of the MCHE. The entrainment of liquid droplets is frequently observed in the annular flow owing to additional shear force caused by oxygen flowing through the MCHE. In addition, the dominant flow patterns are the bubbly slug flow at $Q_{Oxy} \leq 6$ sccm and the annular flow at $Q_{Oxy} \geq 8$ sccm.

(3) The thermal images of the reformer indicate that the POM reaction is more intense near the outlet and the high temperature region expands from the outlet to inlet regions with time until the steady state is reached.

In conclusion, the present study reveals that the employment of IR thermography with proper calibration facilitates real-time temperature monitoring, which enables understanding the distribution of the reforming reaction and its evolution through the reformer until approaching the steady state. The data obtained in the present study may provide a base for theoretical and numerical analyses for the progress of temperature and reforming reaction. The present results also demonstrate that the micro evaporator may effectively use the heat produced from the exothermic POM reaction and provide low-temperature hydrogen for possible application in PEMFC and DMFC.

Acknowledgments

This work was supported by the Ministry of Science and Technology, Taiwan (grant number: 104-3113-E-007-002 and 103-2221-E-007-112-MY3).

REFERENCES

[1] Mekhilef S, Saidur R, Safari A. Comparative study of different fuel cell technologies. Renew Sustain Energy Rev 2012;16:981–9.
[2] Kirubakaran A, Jain S, Nema RK. A review on fuel cell technologies and power electronic interface. Renew Sustain Energy Rev 2009;13:2430–40.
[3] Sharaf OZ, Orhan MF. An overview of fuel cell technology: fundamentals and applications. Renew Sustain Energy Rev 2014;32:810–53.
[4] Avgouropoulos G, Paxinou A, Neophytides S. In situ hydrogen utilization in an internal reforming methanol fuel cell. Int J Hydrogen Energy 2014;39:18103–8.
[5] Yang M, Jiao F, Li S, Li H, Chen G. A self-sustained, complete and miniaturized methanol fuel processor for proton exchange membrane fuel cell. J Power Sources 2015;287:100–7.
[6] Wang HS, Huang KY, Huang YJ, Su YC, Tseng FG. A low-temperature partial-oxidation-methanol micro reformer with high fuel conversion rate and hydrogen production yield. Appl Energy 2015;138:21–30.
[7] Chein RY, Chen YC, Lin YS, Chung JN. Hydrogen production using integrated methanol-steam reforming reactor with various reformer designs for PEM fuel cells. Int J Energy Res 2012;36:466–76.
[8] Huang CC, Huang YJ, Wang HS, Tseng FG, Su YC. A well-dispersed catalyst on porous silicon micro-reformer for enhancing adhesion in the catalyst-coating process. Int J Hydrogen Energy 2014;39:7753–64.
[9] Kim T, Kwon S. MEMS fuel cell system integrated with a methanol reformer for a portable power source. Sens Actuators A 2009;154:204–11.
[10] Hsueh CY, Chu HS, Yan WM, Chen CH. Transport phenomena and performance of a plate methanol steam micro-reformer with serpentine flow field design. Appl Energy 2010;87:3137–47.
[11] Jang JY, Huang YX, Cheng CH. The effects of geometric and operating conditions on the hydrogen production performance of a micro-methanol steam reformer. Chem Eng Sci 2010;65:5495–506.
[12] Lee CY, Lee SJ, Shen CC, Yeh CT, Chang CC, Chang YM. In-situ measurement of the local temperature distributions for the steam reforming of a methanol micro reformer by using flexible micro temperature sensors. Int J Hydrogen Energy 2011;36:2869–76.
[13] Gould BD, Ramamurti R, Osland CR, Swider-Lyons KE. Assessing fuel-cell coolant flow fields with numerical models and infrared thermography. Int J Hydrogen Energy 2014;39:14061–70.
[14] Cumming DJ, Elder RH. Thermal imaging of solid oxide cells operating under electrolysis conditions. J Power Sources 2015;280:387–92.
[15] Tachikawa Y, Sugimoto J, Takada M, Kawabata T, Lyth SM, Shiratori Y, et al. In operando visualization of SOFC electrodes by thermography and visible light imaging. ECS Electrochem Lett 2015;4:F61–4.
[16] Zhang Z, Yuan W, Deng J, Tang Y, Li Z, Tang K. Methanol catalytic micro-combustor with pervaporation-based methanol supply system. Chem Eng J 2016;283:982–91.
[17] Bender G, Felt W, Ulsh M. Detecting and localizing failure points in proton exchange membrane fuel cells using IR thermography. J Power Sources 2014;253:224–9.
[18] Das PK, Weber AZ, Bender G, Manak A, Bittinat D, Herring AM, et al. Rapid detection of defects in fuel-cell electrodes using infrared reactive-flow-through technique. J Power Sources 2014;261:401–11.
[19] Asghari S, Fouladi B, Masaeli N, Imani BF. Leak diagnosis of polymer electrolyte membrane fuel cell stacks. Int J Hydrogen Energy 2014;39:14980–92.
[20] Gade R, Moeslund TB. Thermal cameras and applications: a survey. Mach Vis Appl 2014;25:245–62.
[21] Usamentiaga R, Venegas P, Guerediaga J, Vega L, Molleda J, Bulnes FG. Infrared thermography for temperature measurement and non-destructive testing. Sensors 2014;14:12305–48.
[22] Lee KY, Shen CC, Huang YJ. Enhancement of partial oxidation of methanol reaction over CuZn catalyst by Mn promoter. Ind Eng Chem Res 2014;53:12622–30.
[23] Lu CT, Pan C. Stabilization of flow boiling in microchannel heat sinks with a diverging cross-section design. J Micromech Microeng 2008;18:075035.
[24] Lee PC, Pan C. Boiling heat transfer and two-phase flow of water in a single shallow microchannel with a uniform or diverging cross section. J Micromech Microeng 2008;18:025005.
[25] Park DE, Kim T, Kwon S, Kim CK, Yoon E. Micromachined methanol steam reforming system as a hydrogen supplier for portable proton exchange membrane fuel cells. Sens Actuators A 2007;135:58–66.
[26] Kwon O, Yoon DH, Kim JJ. Silicon-based miniaturized reformer with methanol catalytic burner. Chem Eng J 2008;140:466–72.
[27] Kim T. Micro methanol reformer combined with a catalytic combustor for a PEM fuel cell. Int J Hydrogen Energy 2009;34:6790–8.
[28] Falcão DS, Oliveira VB, Rangel CM, Pinto AMFR. Review on micro-direct methanol fuel cells. Renew Sustain Energy Rev 2014;34:58–70.
[29] Suo C, Zhang W, Wu G, Wang H, Quan X. Silicon-based micro direct methanol fuel cell stack to power portable devices using MEMS technology. Int Ferroelectr Int J 2014;153:133–9.
[30] Hur JI, Kim CJ. Miniature fuel-cell system complete with on-demand fuel and oxidant supply. J Power Sources 2015;274:916–21.

[31] Lee CY, Weng FB, Huang YP, Chang CP, Cheng CK. Real-time monitoring of internal temperature and voltage of high-temperature fuel cell stack. Electrochim Acta 2015;161:413–9.
[32] Chen WH, Shen CT. Partial oxidation of methanol over a Pt/Al_2O_3 catalyst enhanced by sprays. Energy 2016;106:1–12.
[33] Fu BR, Lin PH, Tsou MS, Pan C. Flow pattern maps and transition criteria for flow boiling of binary mixtures in a diverging microchannel. Int J Heat Mass Transf 2012;55:1754–63.
[34] Liu TL, Fu BR, Pan C. Boiling two-phase flow and efficiency of co- and counter-current microchannel heat exchangers with gas heating. Int J Heat Mass Transf 2012;55:6130–41.
[35] Liu TL, Fu BR, Pan C. Boiling heat transfer of co- and counter-current microchannel heat exchangers with gas heating. Int J Heat Mass Transf 2013;56:20–9.